

Citation for published version:

Ma, J, Li, W, Morgan, B, wiatowska, J, Baddour-Hadjean, R, Body, M, Legein, C, Borkiewicz, O, Leclerc, S, Groult, H, Lantelme, F, Laberty-Robert, C & Dambournet, D 2018, 'Lithium Intercalation in Anatase Titanium Vacancies and the Role of Local Anionic Environment', *Chemistry of Materials*, vol. 30, no. 9, pp. 3078–3089. <https://doi.org/10.1021/acs.chemmater.8b00925>

DOI:

[10.1021/acs.chemmater.8b00925](https://doi.org/10.1021/acs.chemmater.8b00925)

Publication date:

2018

Document Version

Peer reviewed version

[Link to publication](#)

This document is the Accepted Manuscript version of a Published Work that appeared in final form in *Chemistry of Materials*, copyright © American Chemical Society after peer review and technical editing by the publisher. To access the final edited and published work see <https://doi.org/10.1021/acs.chemmater.8b00925>.

University of Bath

Alternative formats

If you require this document in an alternative format, please contact:
openaccess@bath.ac.uk

General rights

Copyright and moral rights for the publications made accessible in the public portal are retained by the authors and/or other copyright owners and it is a condition of accessing publications that users recognise and abide by the legal requirements associated with these rights.

Take down policy

If you believe that this document breaches copyright please contact us providing details, and we will remove access to the work immediately and investigate your claim.

Lithium Intercalation in Anatase Titanium Vacancies and the Role of Local Anionic Environment

Jiwei Ma,^{*,†,‡} Wei Li,[†] Benjamin J. Morgan,[#] Jolanta Światowska,^{||} Rita Baddour-Hadjean,[§] Monique Body,[⊥] Christophe Legein,[⊥] Olaf J. Borkiewicz,[▽] Sandrine Leclerc,[†] Henri Groult,[†] Frédéric Lantelme,[†] Christel Laberty-Robert,^{◇,Δ} and Damien Dambournet^{*,†,Δ}

[†]Sorbonne Université, CNRS, Physico-chimie des électrolytes et nano-systèmes interfaciaux, PHENIX, F-75005 Paris, France

[‡]Institute of New Energy for Vehicles, School of Materials Science and Engineering, Tongji University, Shanghai 201804, China

[#]Department of Chemistry, University of Bath, BA2 7AY Bath, United Kingdom

^{||}PSL Research University, CNRS – Chimie ParisTech, Institut de Recherche de Chimie Paris (IRCP), 11 rue Pierre et Marie Curie, 75005 Paris, France

[§]Institut de Chimie et des Matériaux Paris-Est, GESMAT, UMR 7182, CNRS-Université Paris Est, 2 rue Henri Dunant 94320 Thiais France

[⊥]Le Mans Université-CNRS, IMMM, UMR 6283, Institut des Molécules et Matériaux du Mans, Avenue Olivier Messiaen, 72085 Le Mans, Cedex 9, France

[▽]X-ray Science Division, Advanced Photon Source, Argonne National Laboratory, Argonne, Illinois 60439, USA

[◇]Sorbonne Université, CNRS, Collège de France, Laboratoire de Chimie de la Matière Condensée de Paris, F-75005 Paris, France

^ΔRéseau sur le Stockage Electrochimique de l'Energie (RS2E), FR CNRS 3459, 80039 Amiens cedex, France

ABSTRACT: The structure of bulk and non-defective compounds is generally described with crystal models built from well mastered techniques such the analysis of an x-ray diffractogram. The presence of defects, such as cationic vacancies, locally disrupt the long-range order, with the appearance of local structures with order extending only a few nanometers. To probe and describe the electrochemical properties of cation-deficient anatase, we investigated a series of materials having different concentrations of vacancies, i.e., $\text{Ti}_{1-x-y}\square_{x+y}\text{O}_{2-4(x+y)}\text{F}_{4x}(\text{OH})_{4y}$, and compared their properties with respect to defect-free stoichiometric anatase TiO_2 . At first, we characterized the series of materials $\text{Ti}_{1-x-y}\square_{x+y}\text{O}_{2-4(x+y)}\text{F}_{4x}(\text{OH})_{4y}$ by means of pair distribution function (PDF), ^{19}F nuclear magnetic resonance (NMR), Raman and x-ray photoelectron spectroscopies, to probe the compositional and structural features. Secondly, we characterized the insertion electrochemical properties vs. metallic lithium where we emphasized the beneficial role of the vacancies on the cyclability of the electrode under high C-rate, with performances scaling with the concentration of vacancies. The improved properties were explained by the change of the lithium insertion mechanism due to the presence of the vacancies, which act as host sites and suppress the phase transition typically observed in pure TiO_2 , and further favor diffusive transport of lithium within the structure. NMR spectroscopy performed on lithiated samples provides evidence for the insertion of lithium in vacancies. By combining electrochemistry and DFT-calculations, we characterized the electrochemical signatures of the lithium insertion in the vacancies. Importantly, we found that the insertion voltage largely depends on the local anionic environment of the vacancy with a fluoride and hydroxide-rich environments, yielding high and low insertion voltages, respectively. This work further supports the beneficial use of defects engineering in electrodes for batteries and provides new fundamental knowledge in the insertion chemistry of cationic vacancies as host sites.

INTRODUCTION

Introducing defects, particularly cationic vacancies, into host intercalation compounds has been shown to be a viable way to modify the electrochemical properties of electrode materials for lithium storage.¹ Works on defect chemistry for battery materials are, however, rare.² Up to now, the stabilization of cation vacancies has been achieved in certain metal oxides

(manganese, iron and vanadium) by synthetic procedures, including oxidative electrodeposition at high current density,³ doping a fraction of the native metal cations with higher oxidation state dopants,⁴⁻⁵ and heating ordered oxides at high temperature in a defect-inducing environment.⁶ Recently, we reported on a novel methodology for modifying the chemical composition of titanium dioxide, which stabilizes cation va-

cancies.⁷⁻⁸ Cation vacancies were introduced by substituting divalent oxides with monovalent fluorides and hydroxides, yielding the general chemical formula $\text{Ti}_{1-x-y}\square_{x+y}\text{O}_{2-4(x+y)}\text{F}_{4x}(\text{OH})_{4y}$, where \square represents a cationic vacancy. When used as an electrode for lithium-ion battery, this compound showed a modified and enhanced Li activity compared to the stoichiometric TiO_2 , illustrating the beneficial effect of defects.

A better understanding of the relationship between defect chemistry and electrochemical performance is an essential task to generalize the use of vacancies in improving Li-ion batteries. Such a task requires the fine characterization of cationic vacancies, which is, however, particularly challenging.

In the present study, we intended to understand how cationic vacancies impact electrochemical properties vs. Li. This work was motivated by the possibility of controlling the vacancy concentration in anatase $\text{Ti}_{1-x-y}\square_{x+y}\text{O}_{2-4(x+y)}\text{F}_{4x}(\text{OH})_{4y}$. We first provide detailed characterization of materials with distinct vacancy concentrations, by means of pair distribution function (PDF), ^{19}F solid-state nuclear magnetic resonance (NMR), Raman spectroscopy, and X-ray photoelectron spectroscopy (XPS) analyses. Thereafter, the role of the cationic vacancies with respect to lithium intercalation properties was studied by electrochemistry, NMR, and DFT calculations, allowing us to identify the electrochemical signatures of lithium intercalation in vacancies. Our work further emphasizes the impact of the anionic environment of the vacancy, with the redox potential decreasing as the local intercalation environment changes from purely fluorinated to purely hydroxylated. Finally, we demonstrate superior lithium transport within vacancy-containing electrode materials, which can be due to the concomitant formation of percolating network favoring the lithium diffusion and the suppression of the phase transition typically observed in pure TiO_2 .

EXPERIMENTAL SECTION

Synthesis. Anatase $\text{Ti}_{1-x-y}\square_{x+y}\text{O}_{2-4(x+y)}\text{F}_{4x}(\text{OH})_{4y}$ featuring different compositions/vacancy concentrations have been prepared following a previously reported method.⁷ Briefly, solvothermal process was carried out in a stainless steel autoclave with a 45 mL Teflon liner cup inside. 1.2 mL aqueous hydrofluoric acid (*CAUTION: HF solutions are highly hazardous, and special protective equipment is required*) solution was added to the mixture of 24.8 mL isopropanol and 4 mL titanium isopropoxide in the Teflon liner cup. After sealing the autoclave, the mixed solution was heated inside an oven at different temperatures, *i.e.*, 90 °C, 110 °C and 130 °C for 12 h. After cooling down to room temperature, the obtained white precipitate was washed with ethanol and centrifuged, then dried at 100 °C under air for 10 h. For comparison purpose, anatase TiO_2 was synthesized without HF.

$\text{Ti}_{1-x-y}\square_{x+y}\text{O}_{2-4(x+y)}\text{F}_{4x}(\text{OH})_{4y}$ samples were further outgassed at 150 °C overnight under primary vacuum prior to chemical lithiation and electrochemical analyses.

Chemical lithiation were carried out using n-butyl lithium (Sigma-Aldrich, 1.6 M in hexanes).⁹ After dispersing anatase $\text{Ti}_{1-x-y}\square_{x+y}\text{O}_{2-4(x+y)}\text{F}_{4x}(\text{OH})_{4y}$ powder prepared at 90 °C in hexane, an excess of n-butyl lithium (0.2, 0.5 and 0.8 Li^+ per formula unit) was slowly added under stirring. The solution was stirred for 48 hours at room temperature. Lithiation process produces a color change from white to dark purple. After reaction, the products were washed several times with hexane and dried under vacuum. All operations were carried out in an argon-filled glove box.

Characterization methods. X-ray powder diffraction analysis were carried out using a Rigaku Ultima IV X-ray diffractometer equipped with a Cu K α radiation source ($\lambda = 1.54059 \text{ \AA}$).

Total scattering data were collected at the 11-ID-B beamline at the Advanced Photon Source at Argonne National Laboratory, using high energy X-rays ($\lambda = 0.2128 \text{ \AA}$) with high values of momentum transfer $Q_{\text{max}} = 22 \text{ \AA}^{-1}$.¹⁰⁻¹¹ One-dimensional diffraction data were obtained by integrating the raw 2D total scattering data in Fit2D.¹⁵ PDFs, $G(r)$, were extracted from the background and Compton scattering corrected data following Fourier transform within PDFgetX2.¹² The PDFs were subsequently modeled using PDFgui.¹³ PDF peak fitting was performed using Fityk.¹⁴

Raman spectroscopy. Raman spectra were recorded at room temperature using a micro-Raman system with a Labram HR800 (Jobin-yvon-Horiba) spectrometer including Edge filters and equipped for signal detection with a back illuminated charge-coupled device detector (Spex CCD) cooled by Peltier effect to 200 K. A He-Ne laser (633 nm) was used as the excitation source. The spectrum was measured in the back-scattering geometry with a resolution of about 0.5 cm^{-1} . A 100 \times objective was used to focus the laser beam to a spot of $1 \mu\text{m}^2$ size on the sample surface. The laser power was adjusted to 0.2-0.5 mW with neutral filters of various optical densities to avoid local heating of the sample.

X-ray photoelectron spectroscopy. XPS chemical analysis was carried out using a VG ESCALAB 250 spectrometer operating at a residual pressure of 10^{-9} mbar. An Al K α monochromatized radiation ($h\nu = 1486.6 \text{ eV}$) was employed as X-ray source. The spectrometer was calibrated against the reference binding energies (BE) of clean Cu (932.6 eV), Ag (368.2 eV) and Au (84 eV) samples. The photoelectrons were collected at a 90° take-off angle with respect to the substrate surface. Survey and high resolution spectra were recorded with pass energy of 100 and 20 eV, respectively. Binding energies were calibrated versus the C1s signal ($-\text{CH}_2-\text{CH}_2-$ bonds) set at 285.0 eV. The data processing was performed with the Advantage software version 5.954 using a Shirley background and Gaussian/Lorentzian peak shapes at a fixed ratio of 70/30.

^{19}F and ^7Li Solid-State NMR Spectroscopy. ^{19}F and ^7Li solid-state magic angle spinning (MAS) NMR experiments were performed on a Bruker Avance 300 spectrometer operating at 7.0 T (^{19}F and ^7Li Larmor frequencies of 282.2 and 116.7 MHz, respectively), using a 1.3 mm and a 2.5 mm CP-MAS probe head, for recording ^{19}F NMR spectra of the $\text{Ti}_{1-x-y}\square_{x+y}\text{O}_{2-4(x+y)}\text{F}_{4x}(\text{OH})_{4y}$ samples and ^{19}F and ^7Li NMR spectra of the chemically lithiated samples, respectively. The 2.5 mm rotors containing the chemically lithiated samples have been filled in glove-box. The room temperature ^{19}F MAS spectra of the $\text{Ti}_{1-x-y}\square_{x+y}\text{O}_{2-4(x+y)}\text{F}_{4x}(\text{OH})_{4y}$ samples were recorded using a Hahn echo sequence with an interpulse delay equal to one rotor period. The 90° pulse length was set to 1.25 μs or 1.55 μs , and the recycle delay was set to 20 s. The room temperature ^{19}F MAS spectra of the chemically lithiated samples were recorded using a single pulse sequence. The 90° pulse length was set to 1.75 μs , and the recycle delay was set to 10 s. The room temperature ^7Li MAS spectra of the chemically lithiated samples were recorded using a single pulse sequence. The 90° pulse length was set to 0.8 μs , and the recycle delay was set to 10 s. ^{19}F and ^7Li spectra are referenced to CFCl_3 and 1 M LiCl aqueous solution, respectively, and they were fitted by using the DMFit software.¹⁵ ^{19}F solid-state NMR spectroscopy was also used to quantify the fluorine content of the $\text{Ti}_{1-x-y}\square_{x+y}\text{O}_{2-4(x+y)}\text{F}_{4x}(\text{OH})_{4y}$ samples.

$\text{F}_{4x}(\text{OH})_{4y}$ samples following a previously reported method.⁷

Electrochemistry. Electrochemical measurements were carried out with CR2032-type coin cells and three-electrode Swagelok-type cells. The composition of the electrode was 80 wt.% active materials, 10 wt.% Super P, and 10 wt.% polyvinylidene difluoride (PVDF). Copper was used as the current collector. The electrolyte was 1 M LiPF₆ dissolved in a mixture of ethylene carbonate (EC) and dimethyl carbonate (DMC) (1:1, v/v). The cells were assembled and tested with lithium metal as the anode and the reference electrode in the voltage range of 2.5–1.0 V vs. Li⁺/Li.

Density Functional Theory (DFT) calculations. Our density functional theory (DFT) calculations were performed using the code VASP^{16–17}, with valence electrons described by a plane-wave basis with a cutoff of 500 eV. Interactions between core and valence electrons were described using the projector augmented wave (PAW) method¹⁸, with cores of [Ar] for Ti, [He] for O, [He] for F, [He] for Li, and [H⁺] for H. The calculations used the revised Perdew-Burke-Ernzerhof generalized gradient approximation function PBEsol¹⁹, with a Dudarev +*U* correction applied to the Ti d states (GGA+*U*).^{20–21} We used a value of $U_{\text{Ti,d}}=4.2$ eV, which has previously been used to model intercalation of lithium and other metal ions in anatase TiO₂ and TiO₂(B).^{21–24} To model anatase TiO₂, we first performed a full geometry optimisation on a single Ti₄O₈ unit cell, with optimized lattice parameters obtained by fitting a series of constant volume calculations to the Murnaghan equation of state. All subsequent calculations were fixed to the resulting optimised lattice parameters. Intercalation into stoichiometric anatase TiO₂ was modelled using a 3 × 3 × 1 supercell (108 atoms), with a single Li ion inserted at an interstitial site (LiTi₃₆O₇₂). To identify the preferred positions of F[−] and OH[−] anions in relation to a cationic Ti vacancy, we performed a series of calculations in 4×4×2 supercells, with 1 Ti vacancy, and 4 charge compensating *X*₀ species, with *X*=(F, OH), giving cell stoichiometries of Ti₁₂₇O₂₅₂X₄. These calculations agree with previous studies, that reported that fluoride ions preferentially occupy sites adjacent to the titanium vacancy^{7, 25}, in equatorially-coordinated sites. We find the same trend for OH units (**Figures S11 and S12, Supporting Information**). Intercalation into Ti_{1-x-y}□_{x+y}O_{2-4(x+y)}F_{4x}(OH)_{4y} was modelled using 3 × 3 × 1 supercells, with 1 Ti vacancy, and 4 charge compensating *X*₀ species (*X*=F, OH) occupying the four equatorial anion sites adjacent to the vacancy. Lithium intercalation energies were calculated for 4*X*=(4F, 3F+OH, 2F+2OH, F+3OH, and 4OH). In the case of 4*X*=2F+2OH, we considered

like anions arranged in adjacent (cis) and opposite (trans) equatorial site pairs.

Individual calculations were deemed optimised when all atomic forces were smaller than 0.01 eV Å^{−1}. All calculations were spin polarized, and used a 4 × 4 × 2 Monkhorst-Pack grid for sampling *k*-space in the single unit cell, a 2 × 2 × 2 grid for the 3 × 3 × 1 cells, and only the gamma-point for the 4 × 4 × 2 cells. To calculate intercalation energies, reference calculations for metallic Li was performed using the same convergence criteria as above. We considered a 2-atom cell for Li, with a 16 × 16 × 16 Monkhorst-Pack grid for *k*-space sampling. A data set containing all DFT calculation inputs and outputs is available at the University of Bath Data Archive²⁶, published under the CC-BY-SA-4.0 license. Analysis scripts containing intercalation energy calculations, and code to produce Figure 9 are available as an open-source repository as reference [27], published under the MIT license.

RESULTS AND DISCUSSION

Chemical and physical characterizations.

To control the vacancy concentration in anatase Ti_{1-x-y}□_{x+y}O_{2-4(x+y)}F_{4x}(OH)_{4y}, we performed solvothermal synthesis at three different temperature that are 90, 110 and 130 °C.²⁸ The phase purity was confirmed by x-ray diffraction analysis revealing similar patterns characteristic of tetragonal symmetry (*I*₄₁/amd space group) of anatase crystal structure (**Figure S1, Supporting Information**). To determine the chemical composition of the series of samples, we assessed the vacancy content by structural analysis of total scattering data, evaluated the fluorine content using solid-state ¹⁹F NMR and the OH content was deduced according to the general chemical formula Ti_{1-x-y}□_{x+y}O_{2-4(x+y)}F_{4x}(OH)_{4y}.

Structural analysis was performed by measuring total scattering data from which we obtained the pair distribution function, a technique suitable to study nanostructured materials at the atomic scale.²⁹ To assess the titanium vacancy concentration, we used and compared two approaches that are (i) the real-space refinement of PDF data and (ii) individual peaks fitting. First, PDF data were refined against structural model based on the tetragonal symmetry of anatase using a real-space refinement (**Figure 1a and Table 1**). The refinement of the Ti (4a Wyckoff site) rate occupancy confirmed that the titanium vacancy concentration decreases upon increasing the synthesis temperature.²⁸ All the samples show similar unit cell parameters values and close particle sizes (coherence length).²⁸

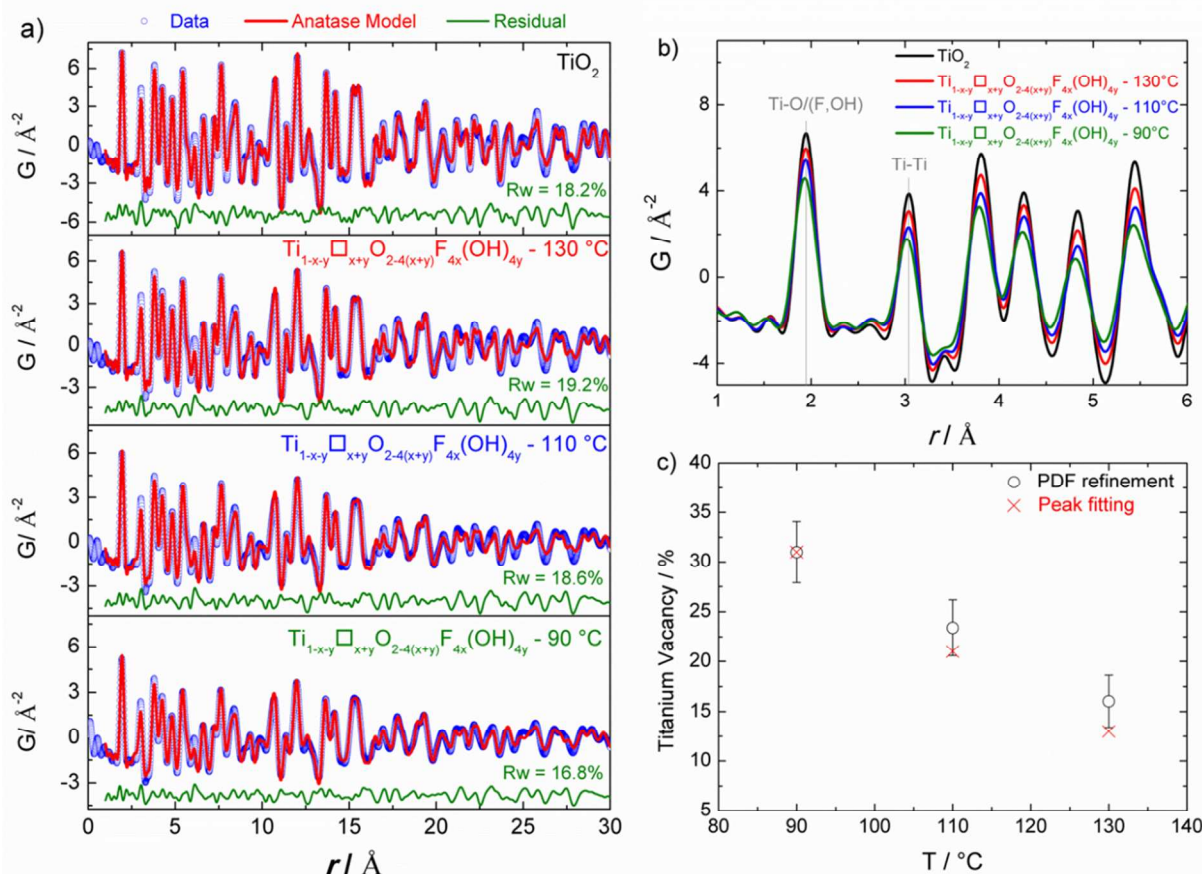


Figure 1. (a) PDF refinements of anatase TiO₂ and Ti_{1-x-y}□_{x+y}O_{2-4(x+y)}F_{4x}(OH)_{4y} prepared at 90 °C, 110 °C and 130 °C. (b) Zoom on the short-range order of PDF data for anatase samples. (c) Determination of the titanium vacancy concentration using real-space refinement and peak fitting for anatase Ti_{1-x-y}□_{x+y}O_{2-4(x+y)}F_{4x}(OH)_{4y}.

To determine the vacancy concentration, we also used the intensity of the peak located at 1.93 Å corresponding to Ti-O/(F,OH) bond length (Figure 1b). Because the intensity of a PDF peak is related to the atomic density, atom occupancy can be deduced by comparing peak intensity with respect to a stoichiometric sample. Using the first peak intensity, we obtained Ti occupancy of 69, 79 and 87 % for the samples prepared at 90, 110 and 130 °C, respectively. A comparison between the vacancies content assessed by real-space refinement and peak fitting (Figure 1c) shows a good agreement for high vacancy content while we expect that peak fitting becomes more accurate for low concentration vacancy containing materials.³⁰

Table 1. Structural parameters obtained by real-space refinement of the PDF data of anatase TiO₂ and Ti_{1-x-y}□_{x+y}O_{2-4(x+y)}F_{4x}(OH)_{4y} samples prepared at 90 °C, 110 °C and 130 °C.

Samples	Lattice constant (Å)	Ti occ.	O occ.	Coherecence length (nm)
TiO ₂	a=b=3.788(1) c=9.489(2)	1.00(1)	1.00(1)	6.8(3)
T= 90 °C	a=b=3.795(1) c=9.489(5)	0.69(3)	1.00(1)	4.8(2)
T= 110 °C	a=b=3.791(1) c=9.491(4)	0.77(3)	1.00(1)	5.5(2)
T= 130 °C	a=b=3.789(1) c=9.494(5)	0.84(3)	1.00(1)	6.5(2)

Fluorine was quantified by ¹⁹F NMR for samples prepared at different temperatures (Table 2). Upon increasing the reaction temperature, the weight percentage of fluorine decreases.²⁸ Chemical compositions were determined by using the general chemical formula Ti_{1-x-y}□_{x+y}O_{2-4(x+y)}F_{4x}(OH)_{4y} (Table 2) where the fluorine and vacancy contents were assessed as aforementioned.

Table 2. Estimated vacancy concentration (□), fluorine content and chemical composition of anatase Ti_{1-x-y}□_{x+y}O_{2-4(x+y)}F_{4x}(OH)_{4y} samples prepared at different temperatures.

T (°C)	□	F (wt%)	Composition
90	0.31	13.3	Ti _{0.69} □ _{0.31} O _{0.76} F _{0.48} (OH) _{0.76}
110	0.21	11.9	Ti _{0.79} □ _{0.21} O _{1.16} F _{0.44} (OH) _{0.40}
130	0.13	8.8	Ti _{0.87} □ _{0.13} O _{1.48} F _{0.36} (OH) _{0.16}

Insight into the fluorine local environments in Ti_{1-x-y}□_{x+y}O_{2-4(x+y)}F_{4x}(OH)_{4y} samples was obtained using ¹⁹F solid-state MAS NMR spectroscopy (Figure 2). The spectra show three distinct lines that were previously assigned to fluorine in the vicinity of different numbers of titanium atoms and titanium vacancies, i.e., species Ti₃-F, Ti₂□-F and Ti□₂-F.⁷ Upon increasing the reaction temperature from 90 °C to 130 °C, the relative intensities of the ¹⁹F NMR lines assigned to the species Ti₃-F (from ≈ 3 % to ≈ 5 %) and Ti₂□-F (from

≈ 60 % to ≈ 65 %) increase, whereas the relative intensity of the ^{19}F NMR lines assigned to the species $\text{Ti}_2\text{□}-\text{F}$ (from ≈ 37 % to ≈ 30 %) decreases (Figures S2-4, Tables S1-3, Supporting Information, Table 3). The concentrations of these species point toward a preferential localization of F atoms close to vacancies. Moreover, the average number of neighboring Ti atoms of the F atoms increases only slightly, from ≈ 1.66 to ≈ 1.74, when the reaction temperature increases from 90 °C to 130 °C, whereas the amount of titanium vacancies decreases from 0.31 to 0.13. Accordingly, the average number of neighboring Ti atoms of the O atoms and OH groups increases from 2.20 to 2.80 in relation with the increase of the O/(O+OH) ratio (Table 3).

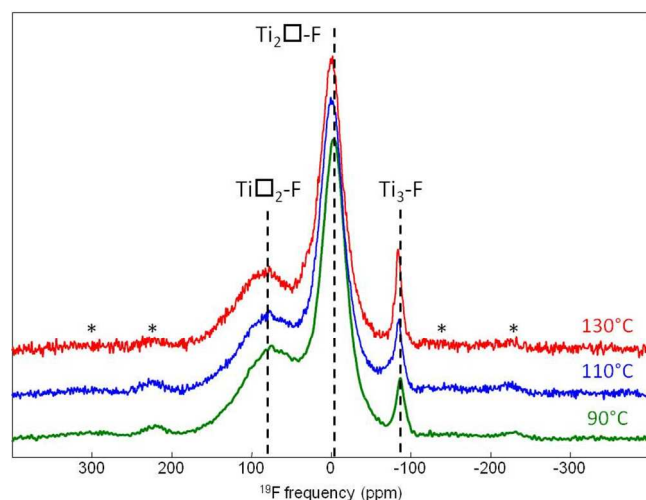


Figure 2. ^{19}F solid-state MAS (64 kHz) NMR spectra of $\text{Ti}_{1-x-y}\text{□}_{x+y}\text{O}_{2-4(x+y)}\text{F}_{4x}(\text{OH})_{4y}$ samples prepared at 90 °C ($\text{Ti}_{0.69}\text{□}_{0.31}\text{O}_{0.76}\text{F}_{0.48}(\text{OH})_{0.76}$, green), 110 °C ($\text{Ti}_{0.79}\text{□}_{0.21}\text{O}_{1.16}\text{F}_{0.44}(\text{OH})_{0.40}$, blue) and 130 °C ($\text{Ti}_{0.87}\text{□}_{0.13}\text{O}_{1.48}\text{F}_{0.36}(\text{OH})_{0.16}$, red). The dashed lines indicate the three NMR lines corresponding to the three-fluorine species occurring in these samples.

Table 3. Estimated proportions of fluorine species (%), average F coordination number (F CN), O/(O+OH) ratio and O(OH) coordination number (O(OH) CN) of anatase $\text{Ti}_{1-x-y}\text{□}_{x+y}\text{O}_{2-4(x+y)}\text{F}_{4x}(\text{OH})_{4y}$ samples.

Sample	$\text{Ti}_3\text{-F}$	$\text{Ti}_2\text{□-F}$	$\text{Ti□}_2\text{-F}$	F CN	O/(O+OH)	O(OH) CN
$\text{Ti}_{0.69}\text{□}_{0.31}\text{O}_{0.76}\text{F}_{0.48}(\text{OH})_{0.76}$	2.6	60.5	37.0	1.66	0.50	2.20
$\text{Ti}_{0.79}\text{□}_{0.21}\text{O}_{1.16}\text{F}_{0.44}(\text{OH})_{0.40}$	4.3	66.0	29.7	1.75	0.74	2.55
$\text{Ti}_{0.87}\text{□}_{0.13}\text{O}_{1.48}\text{F}_{0.36}(\text{OH})_{0.16}$	4.6	64.8	30.6	1.74	0.90	2.80

Raman spectroscopy is a sensitive tool to detect the structural distortions at the scale of the chemical bond. According to the factor group analysis³¹⁻³², six fundamental transitions are expected in the Raman spectrum of anatase, with the following wavenumbers³²⁻³³: $\text{E}_g(1)$ at 144 cm^{-1} , $\text{E}_g(2)$ at 197 cm^{-1} , $\text{B}_{1g}(1)$ at 399 cm^{-1} , $\text{B}_{1g}(2)$ at 519 cm^{-1} , A_{1g} at 513 cm^{-1} and $\text{E}_g(3)$ at 638 cm^{-1} . The overlapping between $\text{B}_{1g}(2)$ and A_{1g} prevents the detection of the weaker A_{1g} component in unpolarized measurements at room temperature. The doubly de-

generate E_g modes involve atom displacements perpendicular to the c axis, while for the other modes, atoms move parallel to the c axis.^{31-32, 34} Most of the modes are predicted to involve both Ti and O atom displacements, except the $\text{B}_{1g}(1)$ that is dominated by Ti atom motions and the A_{1g} that is a pure oxygen vibration.³⁴⁻³⁶

Raman phonon modes belonging to anatase TiO_2 phase (tetragonal D^{194h}_{14} ($\text{I4}_1/\text{amd}$) space group) are clearly identified for the $\text{Ti}_{1-x-y}\text{□}_{x+y}\text{O}_{2-4(x+y)}\text{F}_{4x}(\text{OH})_{4y}$ samples (Figure 3a). While TiO_2 exhibits the five characteristic Raman bands at 143, 196, 397, 517 and 639 cm^{-1} , several changes can be detected upon increasing the vacancy concentration: the $\text{E}_g(1)$ Raman peak is continuously broadened and blue-shifted (Figure 3b); the $\text{B}_{1g}(2)$ and $\text{E}_g(3)$ modes are gradually red-shifted (Figure 3c); the intensity of the $\text{B}_{1g}(1)$ mode decreases progressively.

The most intense $\text{E}_g(1)$ Raman feature is largely investigated in the literature. Many works focus on the variation of position, width and shape of this peak in relation to several effects: defects in the stoichiometry, phonon confinement in nanoparticles, presence of minority phases, pressure and temperature effects, substitutional dopant atoms, O or Ti vacancies, charge carrier density.³⁷ It is not straightforward to distinguish the influence of a single effect among the others because they are often simultaneously present in the investigated sample. However, according to the phonon band structure of anatase³¹, a shift toward higher wavenumbers is expected for the $\text{E}_g(1)$ peak as soon as the fundamental Raman selection rule is relaxed. The presence of a growing local disorder of the perfect crystalline structure in the $\text{Ti}_{1-x-y}\text{□}_{x+y}\text{O}_{2-4(x+y)}\text{F}_{4x}(\text{OH})_{4y}$ samples induced by the presence of titanium vacancies, probably explains the blue shift from 143 to 155 cm^{-1} observed when the titanium vacancy increases from 0 to 0.3 (Figure 3b). On the other hand, the existence of up to three types of anions yielding to multiple X-Ti-X (X = O^{2-} , F $^{-}$, OH^{-}) bending vibrations, may account for the broadening of this peak upon increasing the anionic doping.

The evolution toward lower wavenumbers of the $\text{B}_{1g}(2)$ (517 to 505 cm^{-1}) and $\text{E}_g(3)$ (639 to 628 cm^{-1}) vibrations (Figure 3c) which are mixes of both X-atom and Ti-atom motions, is indicative of an overall decreasing of the Ti-X bond strength. This can be understood by considering the higher electronegativity of the fluorine anion leading to a greater ionicity of the Ti-X bond as compared to the Ti-O bond.

Finally, the progressive intensity decline of the pure Ti-atom $\text{B}_{1g}(1)$ vibration can be easily related to the decreasing amount of vibrating Ti species as the concentration of vacancies increases.

X-ray photoelectron spectroscopy was performed on anatase TiO_2 and $\text{Ti}_{1-x-y}\text{□}_{x+y}\text{O}_{2-4(x+y)}\text{F}_{4x}(\text{OH})_{4y}$ samples (Figure 4). On one hand, the spectrum of TiO_2 displays a Ti $2p_{3/2}$ peak that can be fitted with a single component centered at 458.8 eV characteristic of the binding energy for stoichiometric TiO_2 .³⁸ On the other hand, the Ti $2p_{3/2}$ peak of $\text{Ti}_{1-x-y}\text{□}_{x+y}\text{O}_{2-4(x+y)}\text{F}_{4x}(\text{OH})_{4y}$ samples is red-shifted to 459.1 eV probably due to the presence of the more electronegative environment *i.e.*, F $^{-}$ anion. Furthermore, upon increasing the monovalent doping (F $^{-}$ and OH^{-}), *i.e.*, the heterogeneity of anionic environment in the vicinity of Ti atoms, the full width at half maximum (FWHM) increases from 1.15 to 1.35 eV. In $\text{Ti}_{1-x-y}\text{□}_{x+y}\text{O}_{2-4(x+y)}\text{F}_{4x}(\text{OH})_{4y}$ samples, the F 1s core spectra were reconstructed using a broad single component (FWHM=1.7 eV) centered at 684.6 eV characteristic of Ti-F bonds.³⁹⁻⁴¹ The broadness of the F 1s core peak expresses the various F environments in these samples.

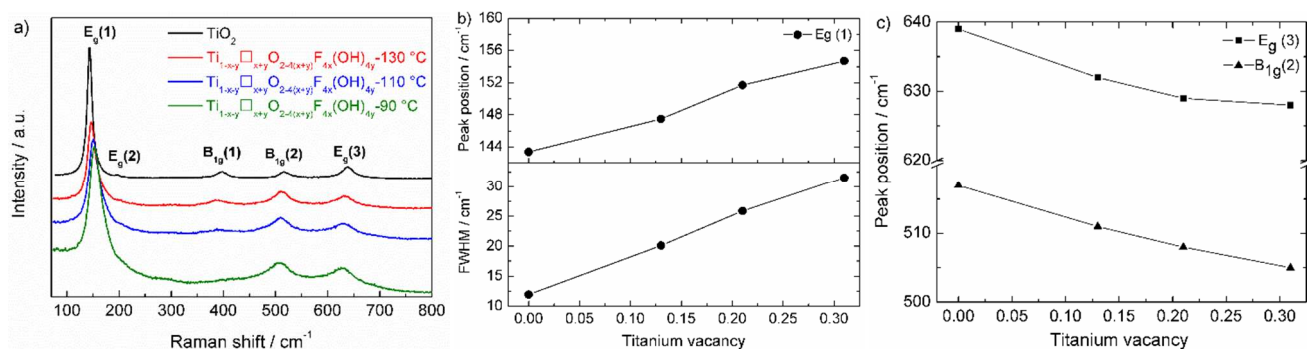


Figure 3. (a) Raman scattering spectra of TiO₂ (reference nanocrystalline anatase powder) and Ti_{1-x-y}□_{x+y}O_{2-4(x+y)}F_{4x}(OH)_{4y} anatase samples prepared at 90 °C, 110 °C and 130 °C, (b) and (c) peak position and full width at half maximum (FWHM) of the TiO₂ and Ti_{1-x-y}□_{x+y}O_{2-4(x+y)}F_{4x}(OH)_{4y} anatase samples as a function of the titanium vacancy concentration.

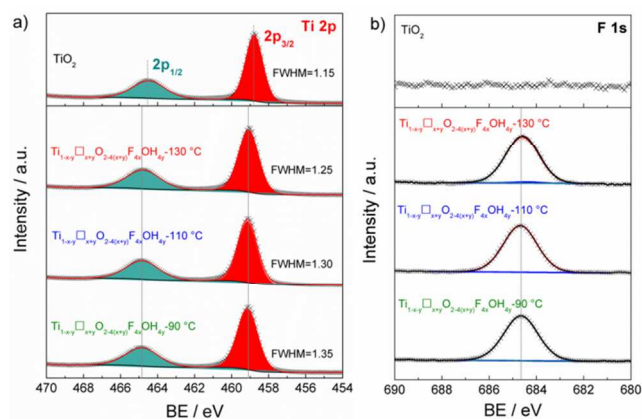


Figure 4. High resolution (a) Ti 2p, and (b) F 1s XPS spectra of TiO₂ and Ti_{1-x-y}□_{x+y}O_{2-4(x+y)}F_{4x}(OH)_{4y} anatase samples prepared at 90 °C, 110 °C and 130 °C.

Electrochemical properties.

The electrochemical properties of anatase Ti_{1-x-y}□_{x+y}O_{2-4(x+y)}F_{4x}(OH)_{4y} were evaluated and compared with the stoichiometric anatase TiO₂ using galvanostatic discharge/charge experiments. **Figure 5** shows the discharge/charge cycles obtained under galvanostatic conditions within a range of 2.5 and 1.0 V at 0.1 C and 1 C rates (note that 1 C = 335 mAh g⁻¹). Under 0.1 C rate, the samples Ti_{1-x-y}□_{x+y}O_{2-4(x+y)}F_{4x}(OH)_{4y} prepared at 90 °C, 110 °C and 130 °C show slightly higher discharge capacities with 255 mAh g⁻¹, 248 mAh g⁻¹ and 241 mAh g⁻¹, respectively (corresponding to 0.76, 0.74 and 0.72 Li⁺ per formula unit), in comparison with 234 mAh g⁻¹ (corresponding to 0.70 Li⁺ per formula unit) for TiO₂. Under 1C rate, the samples Ti_{1-x-y}□_{x+y}O_{2-4(x+y)}F_{4x}(OH)_{4y} prepared at 90 °C, 110 °C and 130 °C maintain high discharge capacities of 229 mAh g⁻¹, 208 mAh g⁻¹ and 174 mAh g⁻¹, respectively (corresponding to 0.68, 0.62 and 0.52 Li⁺ per formula unit). In contrast, a capaci-

ty decreases down to 110 mAh g⁻¹ (corresponding to 0.33 Li⁺ per formula unit) is observed for TiO₂. Strikingly, we noted that the discharge/charge curves at 1C show lower polarization than at 0.1C. Although this point remains unclear, it might be due to a concomitant effect of lower resistivity obtained at lower lithium concentration and/or an effect of the vacancies favoring the diffusion of lithium. Overall, higher capacities are obtained for anatase containing vacancies. Such a trend is also observed for long-term cycling experiments, shown in **Figure 5e**. The samples Ti_{1-x-y}□_{x+y}O_{2-4(x+y)}F_{4x}(OH)_{4y} prepared at 90 °C, 110 °C and 130 °C show stable cycling performance over 500 cycles with superior capacity retention on cycling of 80%, 70% and 62%, respectively, compared to 30% for TiO₂ anatase after 500 cycles.

Intercalation mechanism.

The lithium intercalation mechanism that takes place in anatase Ti_{1-x-y}□_{x+y}O_{2-4(x+y)}F_{4x}(OH)_{4y} and TiO₂ electrodes was first investigated using the quasi-equilibrium voltage obtained by the galvanostatic intermittent titration technique (GITT) shown in **Figure 6**. As expected, a constant voltage plateau is observed for anatase TiO₂ corresponding to the phase transition from tetragonal to orthorhombic Li-rich phase.⁴²⁻⁴⁴ Upon increasing the vacancy concentration, the plateau region characteristic of the phase transition progressively vanishes, indicating a change toward a solid solution behavior. The latter was tentatively explained by the presence of vacancies⁷ acting as additional sites for lithium ions that can minimize the formation of the edge-shared LiO₆ octahedra driving the phase transition.²² In this study, anatase TiO₂ and Ti_{1-x-y}□_{x+y}O_{2-4(x+y)}F_{4x}(OH)_{4y} samples present similar particle size/coherence length suggesting that the presence of titanium vacancies is the predominant factor influencing the lithium storage mechanism, *i.e.*, phase transition vs. solid solution.⁴⁵

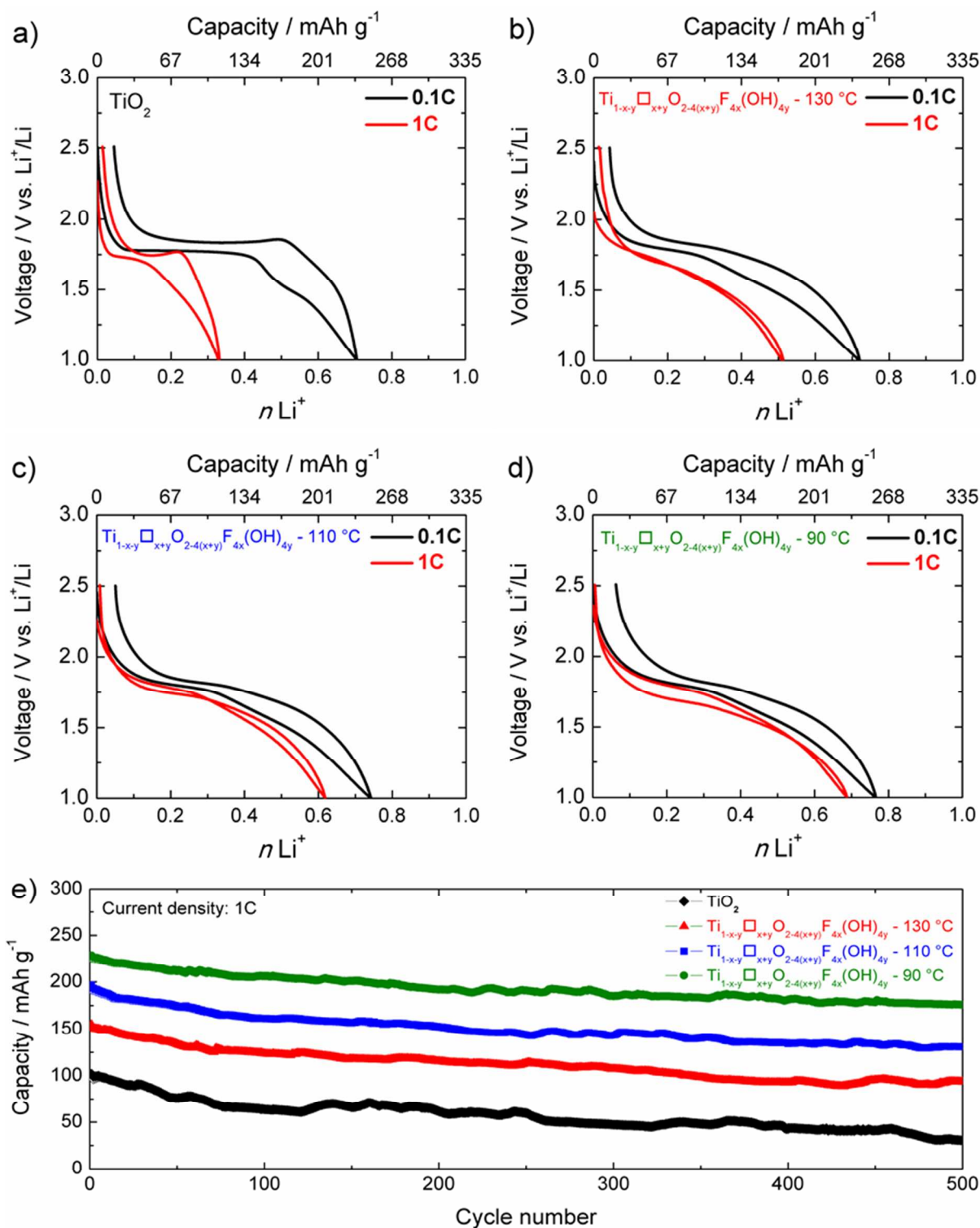


Figure 5. (a, b, c, d) Galvanostatic discharge-charge curves (2nd cycle) at 0.1C and 1C rates, and (e) long cycling performance at 1C rate for anatase TiO_2 and $\text{Ti}_{1-x-y}\text{O}_{x+y}\text{F}_{4x}(\text{OH})_{4y}$ prepared at 130 °C, 110 °C and 90 °C (the cells were activated at 0.1C for the first cycle).

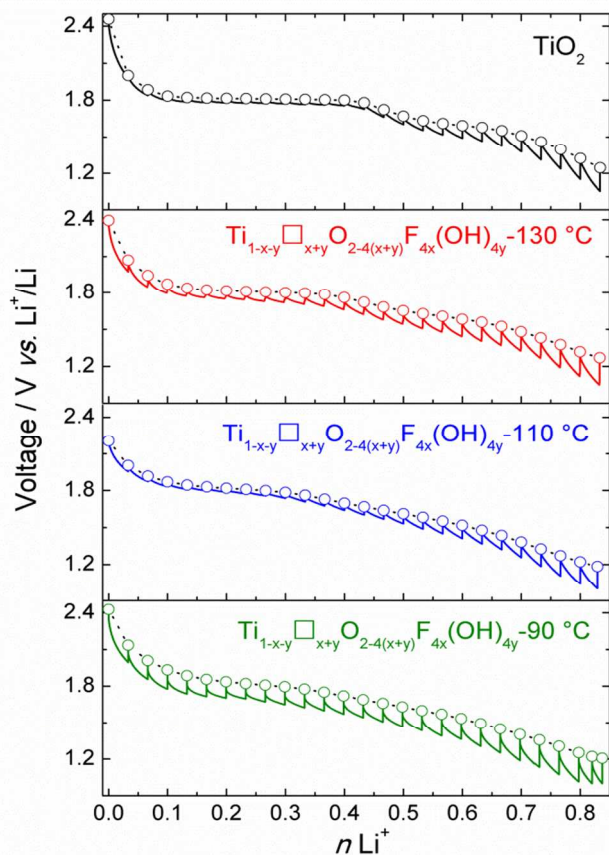


Figure 6. Voltage-composition profiles obtained using the galvanostatic intermittent titration technique (GITT) recorded during the second discharge for anatase TiO_2 and $\text{Ti}_{1-x-y}\square_{x+y}\text{O}_{2-4(x+y)}\text{F}_{4x}(\text{OH})_{4y}$ prepared at 130 °C, 110 °C and 90 °C electrodes.

To attest for the lithium intercalation within the vacancy sites, we used ^{19}F solid state NMR performed on chemically lithiated samples prepared from the sample obtained at 90 °C. Prior to lithiation reactions, the sample was outgassed at 150 °C which induces a modification of the chemical composition from $\text{Ti}_{0.69}\square_{0.31}\text{O}_{0.76}\text{F}_{0.48}(\text{OH})_{0.76}$ to $\text{Ti}_{0.78}\square_{0.22}\text{O}_{1.12}\text{F}_{0.40}(\text{OH})_{0.48}$.⁷ **Figure 7** shows the ^{19}F MAS NMR spectra of the pristine and lithiated samples. Several chemical lithiation were performed at increasing lithium concentrations that are 0.2, 0.5 and 0.8 Li^+ per formula unit (**Figures 7b-d**). ^7Li solid state MAS NMR spectra of the chemically lithiated samples showed that the signal increases when the concentration of n-butyl lithium increases confirming the increasing insertion of lithium (**Figure S5, Supporting Information**). Moreover, we note the presence of LiF upon lithiation as revealed by X-ray diffraction analysis (**Figure S10, Supporting Information**). The ^{19}F MAS NMR spectra of the pristine and lithiated samples (fits are given as **Supporting Information, Figures S6-8 and Tables S5-7**) confirm the presence of LiF and show the appearance of adsorbed F^- ions which suggest that chemical lithiation damages the material. We note that the presence of LiF was not detected by XRD and PDF on electrochemically prepared sample.⁷ Based on the ^{19}F isotropic chemical shift (δ_{iso}) values of the environments $\text{Ti}^{\text{IV}}\square_2\text{-F}$, $\text{Ti}^{\text{IV}}_2\square\text{-F}$ and $\text{Ti}^{\text{IV}}_3\text{-F}$ in $\text{Ti}_{0.78}\square_{0.22}\text{O}_{1.12}\text{F}_{0.40}(\text{OH})_{0.48}$, $\text{Li}_6\text{-F}$ in LiF (-204.3 ppm)⁴⁶ and in TiF_3 (-144.8 ppm, $\text{Ti}^{\text{III}}_2\text{-F}$)²⁴ and on the decrease of the δ_{iso} value of fluoride anions when the number of surrounding cations increases, the insertion of Li^+ ion in a titanium vacancy and/or in an interstitial site and the reduction of a Ti^{4+} ion into a Ti^{3+} ion are both expected to

induce a decrease of the δ_{iso} value of the neighboring fluorine. When the concentration of n-butyl lithium increases, the relative intensities of the NMR resonances of higher (smaller) chemical shift decrease (increase) and the NMR lines assigned to $\text{Ti}^{\text{IV}}\square_2\text{-F}$ and $\text{Ti}^{\text{IV}}_2\square\text{-F}$ vanish (from 0.2 Li^+ per formula unit and from 0.5 Li^+ per formula unit, respectively), evidencing the insertion of lithium in vacancies. However, considering the number of species which may exist (**see discussion in Supporting Information and Table S4**) and the low resolution of the ^{19}F NMR spectra, the assignment of the NMR lines is complex and could not be achieved.

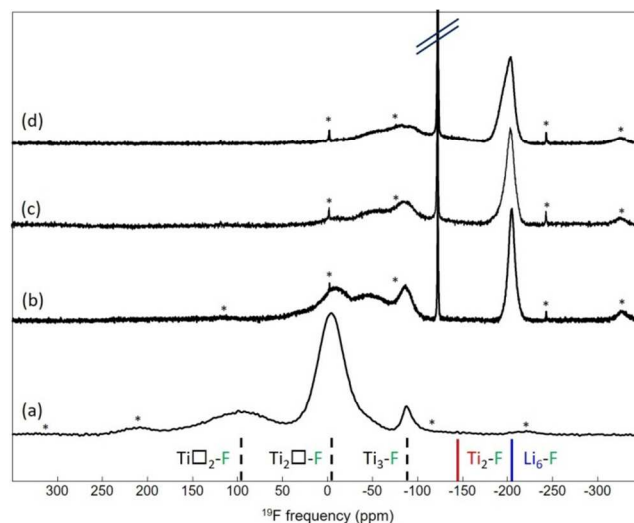


Figure 7. ^{19}F solid-state MAS NMR spectra of (a) $\text{Ti}_{0.78}\square_{0.22}\text{O}_{1.12}\text{F}_{0.40}(\text{OH})_{0.48}$ (60 kHz) and chemically lithiated ((b) 0.2, (c) 0.5 and (d) 0.8 Li^+ per formula unit samples) (34 kHz). The asterisks indicate the main spinning sidebands. The dashed lines indicate the ^{19}F δ_{iso} values of the $\text{Ti}^{\text{IV}}_3\text{-F}$, $\text{Ti}^{\text{IV}}_2\square\text{-F}$, and $\text{Ti}^{\text{IV}}\square_2\text{-F}$ environments in $\text{Ti}_{0.78}\square_{0.22}\text{O}_{1.12}\text{F}_{0.40}(\text{OH})_{0.48}$. Solid lines indicate the ^{19}F δ_{iso} values of the $\text{Ti}^{\text{III}}_2\text{-F}$ environment in TiF_3 and the $\text{Li}_6\text{-F}$ environment in LiF . Ti^{IV} are in black and Ti^{III} are in red. The narrow lines observed on the spectra of the lithiated samples are assigned to adsorbed F^- ions.

Slow scanning linear sweep voltammetry was used to investigate the electrochemical signatures of the lithium insertion in the various host sites of anatase $\text{Ti}_{1-x-y}\square_{x+y}\text{O}_{2-4(x+y)}\text{F}_{4x}(\text{OH})_{4y}$ and TiO_2 . A slow-scan rate of 0.05 mV s^{-1} at the condition approaching equilibrium was applied, which allows excluding the capacitive contribution.⁴⁷ **Figure 8** shows the anodic part of the Li insertion process obtained after one activating cycle. For anatase TiO_2 , the cyclic voltammogram was reconstructed using two signals (signal I and II) at 1.71 and 1.56 V vs. Li^+/Li . The higher redox potential corresponds to the lithium insertion reaction in the interstitial sites of anatase.⁴⁸ The occurrence of a second peak at lower potential can be due to a concentration dependence of lithium insertion in anatase. Particularly, this second peak can be related to the insertion of lithium in the lithium-rich orthorhombic phase $\text{Li}_{0.5}\text{TiO}_2$.⁴⁹

The introduction of Ti vacancies yields significant changes in slow scan rate cyclic voltammograms. Upon increasing the vacancy concentration, we observed the appearance of new redox peaks occurring at a broader potential window. Moreover, the signals I and II were observed at higher potentials ($\Delta E = 0.07$ V) in anatase $\text{Ti}_{1-x-y}\square_{x+y}\text{O}_{2-4(x+y)}\text{F}_{4x}(\text{OH})_{4y}$. Furthermore, the signal II was reconstructed using a broad line suggesting that the lithium insertion occurred in sites featuring different energies which can be related to the heterogeneous anionic environment found in $\text{Ti}_{1-x-y}\square_{x+y}\text{O}_{2-4(x+y)}\text{F}_{4x}(\text{OH})_{4y}$ samples.

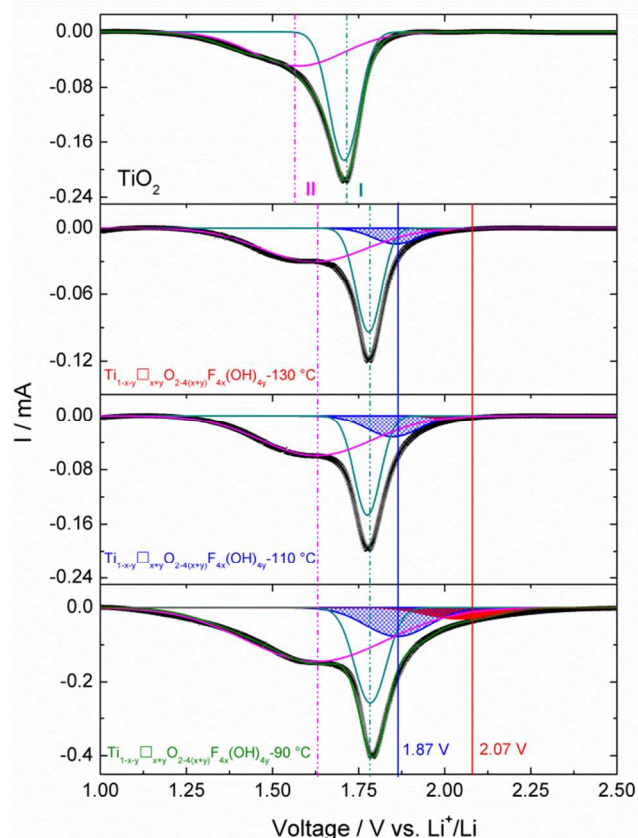


Figure 8. Slow scanning liner sweep voltammeteries of TiO_2 and $\text{Ti}_{1-x-y}\square_{x+y}\text{O}_{2-4(x+y)}\text{F}_{4x}(\text{OH})_{4y}$ anatase prepared at 130 °C, 110 °C and 90 °C electrodes at a scan rate of 0.05 mV s^{-1} (obtained after one activating cycle).

To better understand the effect of local anion environment on the insertion of lithium in anatase $\text{Ti}_{1-x-y}\square_{x+y}\text{O}_{2-4(x+y)}\text{F}_{4x}(\text{OH})_{4y}$, we performed a series of DFT calculations. We have previously calculated insertion energies of lithium at the octahedral interstitial site in stoichiometric anatase TiO_2 , and at titanium vacancies in fluorine-substituted anatase TiO_2 .^{7, 24} For Li insertion into stoichiometric anatase, we found intercalation energy of -1.23 eV. For the cation-deficient anatase TiO_2 system, we considered systems with one single vacancy ($\text{Ti}_{35}\square_{1}\text{O}_{68}\text{F}_4$) and two adjacent vacancies ($\text{Ti}_{126}\square_{2}\text{O}_{248}\text{F}_8$), which gave favorable intercalation energies of -2.68 eV and -2.88 eV, respectively. These more favorable insertion energies translate to higher redox potentials of 2.68 and 2.88 V which are, however, higher than the redox potentials observed in CV, *i.e.*, 1.87 and 2.07 V. To supplement these previous results, we considered the single vacancy system ($\text{Ti}_{35}\square_{1}\text{O}_{68}\text{X}_4$) with X varied from fully fluorinated (with the Ti vacancy coordinated by 2O and 4F), through hydroxyfluorinated (coordination by 2O, xOH, and (4-x)F), to fully hydroxylated (coordination by 2O and 4OH) environments. In each case we consider the four X anions to occupy equatorial sites around the Ti vacancy (see **Supporting Information, Figures S11 and S12**, and the supporting data in the reference [27]). **Figure 9** shows the variation in lithium insertion energies with changes in the local anionic environment surrounding the vacancy. The redox potential progressively drops from 2.68 V for 4F to 1.2 V for 4OH demonstrating a significant impact of the anionic environment on the redox potentials. This result emphasizes the inductive effect of fluoride ions on the redox potential.⁵⁰ The presence of protons, however, tends to decrease the redox potential, which is possibly due to steric effects. The occurrence of a higher potential for the signal I ($\Delta E=0.07$ V) in

anatase $\text{Ti}_{1-x-y}\square_{x+y}\text{O}_{2-4(x+y)}\text{F}_{4x}(\text{OH})_{4y}$ can therefore be explained by the presence of fluoride ions in the vicinity of the interstitial site as revealed by the presence of $\text{Ti}_3\text{-F}$ species observed

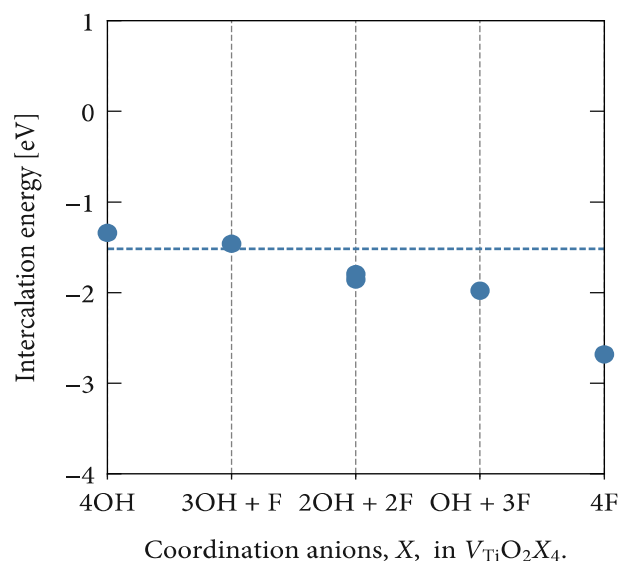


Figure 9. Intercalation energy of lithium in a $\text{Ti}_{35}\square_{1}\text{O}_{68}\text{X}_4$ supercell with $\text{X} = \text{F}, \text{OH}$. The horizontal dashed line shows the intercalation energy for lithium in stoichiometric anatase TiO_2 . *Source:* The data set and code to generate this figure, and the figure file, are available under the MIT licence as part of [ref 27].

Kinetic aspects.

The evolution of the diffusion coefficients for Li^+ in both TiO_2 and $\text{Ti}_{0.78}\square_{0.22}\text{O}_{1.12}\text{F}_{0.40}(\text{OH})_{0.48}$ electrodes was followed during the discharge process (**Figures 10a and d**) using GITT.⁵¹⁻⁵² The variation of the diffusion coefficients as a function of the Li^+ concentration was plotted in **Figures 10b and e**.

At the early stage of lithiation of anatase TiO_2 , the diffusion coefficient decreases from $8.3 \times 10^{-12} \text{ cm}^2 \text{ s}^{-1}$ for $x \sim 0.03 \text{ Li}^+$ to $1 \times 10^{-13} \text{ cm}^2 \text{ s}^{-1}$ for $x \sim 0.2 \text{ Li}^+$. The origin of such a decrease is related to the reduction of Ti^{4+} causing the progressive shortening of the O-O pairs through which Li^+ diffuses, further increasing the site migration barriers.⁵³ Upon increasing x to 0.5 Li^+ , the diffusion coefficient increases back to $2.5 \times 10^{-12} \text{ cm}^2 \text{ s}^{-1}$ which is caused by the structural transition toward the ordered lithiated orthorhombic phase. Thereafter, it further decreases during the solid solution lithiation in the orthorhombic phase. Finally, we observed a subsequent increase of the diffusion coefficient to $9 \times 10^{-13} \text{ cm}^2 \text{ s}^{-1}$ which can be related to a second phase transition toward the Li-rich tetragonal phase. We note that the diffusion coefficients obtained in this study differ from the literature values due to the different thickness of the electrode films.

In the case of $\text{Ti}_{0.78}\square_{0.22}\text{O}_{1.12}\text{F}_{0.40}(\text{OH})_{0.48}$, the evolution of the lithium diffusion coefficient showed less pronounced variation. At the early stage of lithiation, the diffusion coefficient decreases from $8.0 \times 10^{-12} \text{ cm}^2 \text{ s}^{-1}$ for $x \sim 0.03 \text{ Li}^+$ to $4.6 \times 10^{-13} \text{ cm}^2 \text{ s}^{-1}$ for $x \sim 0.26 \text{ Li}^+$. Thereafter, the diffusion coefficient value remains stable with a value of $8.3 \times 10^{-13} \text{ cm}^2 \text{ s}^{-1}$ for $x \sim 0.8 \text{ Li}^+$.

The above-mentioned results clearly show that the crystal structural features such as vacancies largely impact the lithium diffusion. We showed that the presence of vacancies in anatase modifies the insertion mechanism by suppressing the phase transition toward a solid solution behavior. At the early stage of lithiation ($x \sim 0.03$ - 0.2 Li⁺), it is striking how the presence of vacancies that act as host sites can mitigate the structural impact of the Ti⁴⁺ reduction and in turn the migration barriers with a decrease of the diffusion coefficient by a factor of 83 and 10 in anatase TiO₂ and Ti_{0.78}□_{0.22}O_{1.12}F_{0.40}(OH)_{0.48}, respectively. The absence of the phase transition suppresses the large variation of the diffusion coefficient observed for TiO₂ which can be at the origin of the higher rate capability observed for vacancies containing materials.

Thermodynamic considerations.

In order to establish a link between the thermodynamic properties and the electrochemical behavior of the batteries it is worth to introduce the analysis previously developed to describe the lithium insertion in solid substrates.⁵⁴ The electrochemical investigation shows that the studied systems exhibit large deviations from ideality. Then, an activity factor, f_{Li} , must be introduced in the Nernst's equation that binds the open circuit voltage, E , to the concentration of the active material, C_{Li}

$$E = E^0 - \frac{RT}{F} \ln(f_{Li} C_{Li}) \quad (1)$$

where

$$E^0 = \frac{RT}{F} \ln C_{Li}^0 \quad (2)$$

C_{Li}^0 is the concentration of lithium metal. The values of f_{Li} can be deduced from the potential curve E vs. C_{Li} or E vs. n , where the lithium compound is written as TiO₂Li _{n} ; n and C_{Li} are linked through the equation

$$C_{Li} = \frac{n}{V_{TiO_2Li_n}} \quad (3)$$

$V_{TiO_2Li_n}$ is the molar volume of the compound.

The activity factor, f_{Li} , is an important physical value since it represents the excess Gibbs energy (ΔG_{Li}^E) of formation of the lithium insertion in the substrate, which is the heart of the battery operation. For a compound TiO₂Li _{n} , the insertion of one mole of Li, i.e. formation of (TiO₂) _{z} Li (with $z = \frac{1}{n}$) is

$$\Delta G_{Li}^E = -RT \ln f_{Li} \quad (4)$$

the more negative ΔG_{Li}^E is, the more positive the electrode potential is.

The deviation from ideality has a direct influence on the kinetic properties of the battery; indeed the real diffusion driving force is the gradient of the chemical potential and, as shown by Darken,⁵⁵ an enhancement factor, $\zeta = \varphi \left(1 + \frac{d \ln f_{Li}}{d \ln C_{Li}}\right)$ should be introduced in the diffusion equation; then the diffusion flux writes

$$J_{Li} = D \varphi \left(1 + \frac{d \ln f_{Li}}{d \ln C_{Li}}\right) \frac{d C_{Li}}{dx} \quad (5)$$

where D is the chemical diffusion coefficient,⁵⁶ and φ is a damping factor introduced to take account of the thermodynamic properties of the system.^{54,57}

In previous papers⁵⁸⁻⁵⁹, it was shown that a suitable representation of the variation of the activity factor was given by the series:

$$\ln f_{Li} = \sum_{j=1}^n (\ln f_j - \ln f_{j-1}) \operatorname{erfc}\{\psi_i (C_{Li} - C_{Tj})\} \quad (6)$$

$\ln f_j$ is the activity factor corresponding to a plateau of the potential curve, the complementary error function, erfc , was used to describe the change from one factor to the next; C_{Tj} is the concentration at the inflexion point of the potential curve. ψ_i is the steepness of the change of the activity factor around the concentration C_{Tj} (**Table S9, Supporting Information**).

The various parameters $\ln f_i$ and ψ_i were adjusted to obtain a suitable representation of the OCV curves (**Figures 10a and d**): four terms in the sum ($n=4$, Eq.6) were used, the first one (index 1) and the last one (index 4) are relative to the high and very low lithium concentrations respectively. The other two correspond to the operative range of the battery.

These theoretical considerations have a major impact on the analysis of the system:

- The two potential plateaus of the potential curve (clearly visible on the Li-TiO₂ system, (**Figure 10a**) correspond to the composition TiO₂Li_{0.65} and TiO₂Li_{0.3}. In order to consider the implementation of one mole of lithium, the compounds can be written as Li(TiO₂)_{1.54} and Li(TiO₂)_{3.33}. The excess Gibbs energy of formation of that compounds, deduced from the value of the activity coefficient f_2 and f_3 , are: -144 kJ and -156 kJ, respectively.
- The classical formula used to analyze the GITT curves⁵¹⁻⁵² (**Figure 6**) is based on the Fick's law which states that, for an ideal system, the lithium flux J_{Li} is proportional to the concentration gradient:

$$J_{Li} = D_{Fick} \frac{d C_{Li}}{dx} \quad (7)$$

However, in this determination the important departure to ideality of the system was neglected. Then, as shown by the analysis of the diffusion process (Eq. 6), the quantity D_{Fick} is linked to the chemical diffusion coefficient D through the equation:

$$D_{Fick} = \zeta D \quad (8)$$

According to the curves in **Figures 10b and e**, it should be noted that the important variations of the D_{Fick} versus the lithium concentration arise mainly from the thermodynamic properties of the system as shown by the concomitant values of the enhancement factor **Figures 10c and f**.

- For the Li-TiO₂ system, the lithium insertion gives rise to well defined phases, and the transition from one potential plateau to the other is quite sharp that induces a very large change in the enhancement factor; the lithium transport is enhanced by a factor greater than ten (**Figure 10c**). The structural changes in the fluorinated compounds are less marked; the steepness factors become smaller, and various structures can coexist. It results in a more continuous value of the enhancement factor, con-

comitant to a continuous value of the diffusion coefficient D_{Fick} (Figures 10e and f).

The thermodynamic properties of the lithium intercalation into anatase or fluorinated anatase described in the above

study are useful to establish a link between the structural properties of the electrode material and their influence on the electrochemical behavior of the system.

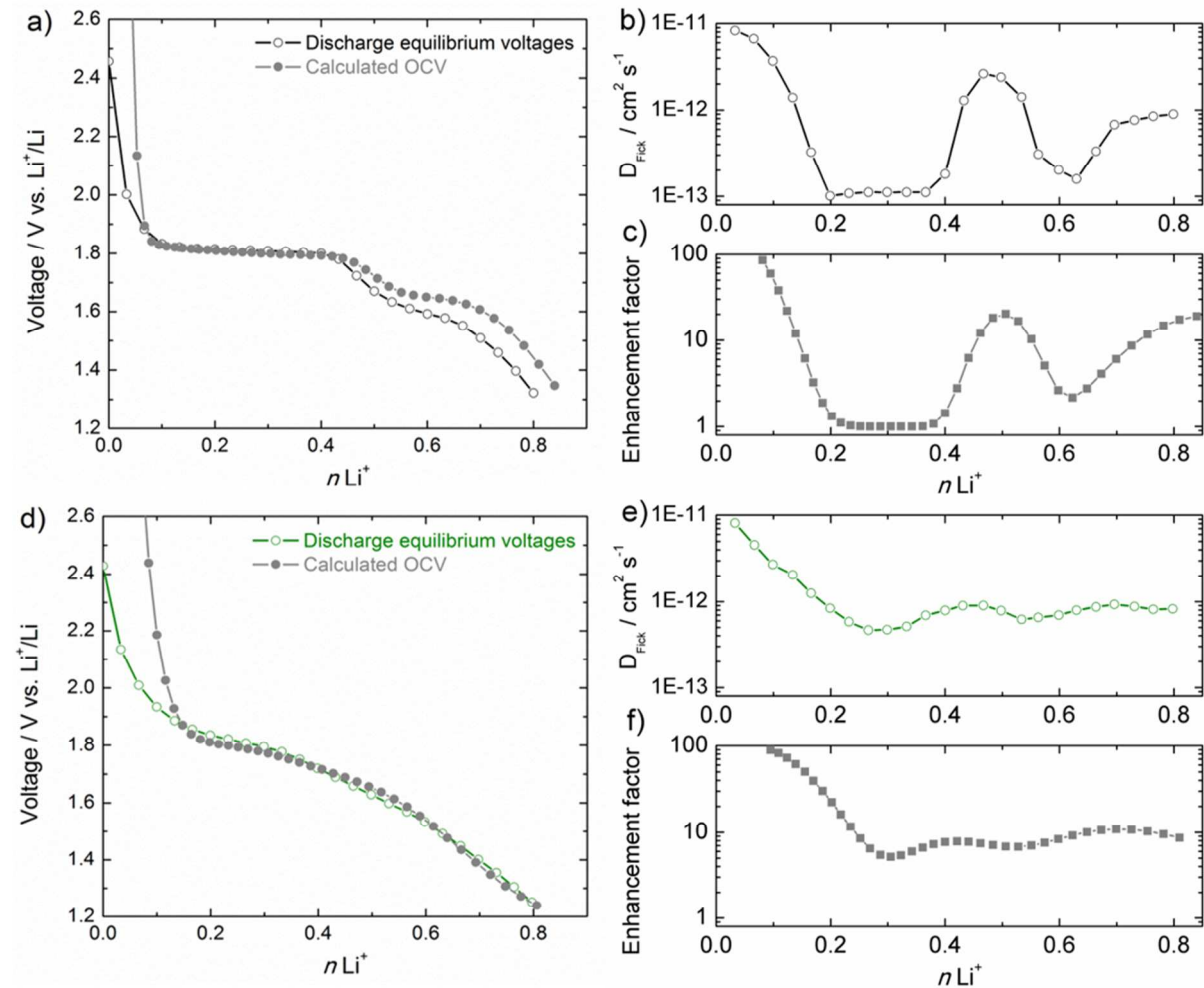


Figure 10. (a) and (d) Equilibrium voltage profiles via GITT and calculated OCV profiles, (b) and (d) extracted diffusion coefficient for TiO_2 and $\text{Ti}_{0.78}\square_{0.22}\text{O}_{1.12}\text{F}_{0.40}(\text{OH})_{0.48}$ electrodes. (c) and (f) corresponding calculated enhancement factor profiles.

CONCLUSION

In this work, we prepared cation-deficient anatase having different concentration of vacancies *i.e.*, $\text{Ti}_{1-x-y}\square_{x+y}\text{O}_{2-4(x+y)}\text{F}_{4x}(\text{OH})_{4y}$ which chemical formulas were determined using PDF analysis (both using real-space refinements and peak fitting methods) and ^{19}F NMR spectroscopy. Raman spectroscopy confirmed the presence of titanium vacancies while x-ray photoelectron spectroscopy attested of the broad anionic heterogeneity in the samples. Galvanostatic experiments showed the beneficial role of the vacancies on the cyclability of the electrode under high C-rate, with performances scaling with the concentration of vacancies. Deeper understanding of the vacancy's insertion chemistry was obtained using low scan rate cyclic voltammetry showing the appearance of new and shifted redox peaks. The assignment of these peaks was done using DFT calculations performed on vacancies featuring fluoride- to hydroxide-rich anionic environment in the vicinity of the vacancy. Moreover, we found that the presence of vacancies favors the diffusion transport of lithium within the structure in part due to the suppression of the phase transition typically encountered in pure TiO_2 . This work further supports the beneficial use of defects engineering in electrode materials for batteries and provides new fundamental knowledge in the insertion chemistry of cationic vacancies as host sites.²⁴

ASSOCIATED CONTENT

Supporting Information. Additional information such as XRD patterns and fits of ^{19}F MAS NMR spectra. This material is available free of charge via the Internet at <http://pubs.acs.org>.

Data Access Statement. The DFT dataset supporting this study is available from the University of Bath Research Data Archive (doi:10.15125/BATH-00473) [26], published under the CC-BY-SA-40 license. This dataset contains all input parameters and output files for the VASP DFT calculations, and Python scripts for collating the relevant data used in our analysis. Jupyter notebooks containing code to produce Figs 9, S11 & S12 are available (Ref [27], doi: 10.5281/zenodo.1181872), published under the MIT license.

AUTHOR INFORMATION

Corresponding Authors

*Email: jiwei.ma@tongji.edu.cn (JM)
damien.dambournet@sorbonne-universite.fr (DD)

Notes

The authors declare no competing financial interests.

ACKNOWLEDGMENT

The research leading to these results has received funding from the French National Research Agency under Idex@Sorbonne University for the Future Investments program (No. ANR-11-IDEX-0004-02). Region Ile-de-France is acknowledged for partial funding of the XPS equipment. This research used resources of the Advanced Photon Source, a U.S. Department of Energy (DOE) Office of Science User Facility operated for the DOE Office of Science by Argonne National Laboratory under Contract No. DE-AC02-06CH11357. B. J. M. acknowledges support from the Royal Society (UF130329). DFT calculations were performed using the Balena High Performance Computing Service at the University of Bath, and using the ARCHER supercomputer, with access through membership of the UK's HPC Materials Chemistry Consortium, funded by EPSRC grant EP/L000202.

REFERENCES

- Hahn, B. P.; Long, J. W.; Rolison, D. R., Something from Nothing: Enhancing Electrochemical Charge Storage with Cation Vacancies. *Acc. Chem. Res.* **2013**, *46*, 1181-1191.
- Maier, J., Review—Battery Materials: Why Defect Chemistry? *J. Electrochem. Soc.* **2015**, *162*, A2380-A2386.
- Sarciaux, S.; Le Gal La Salle, A.; Verbaere, A.; Piffard, Y.; Guyomard, D., $\gamma\text{-MnO}_2$ for Li batteries: Part I. $\gamma\text{-MnO}_2$: Relationships between synthesis conditions, material characteristics and performances in lithium batteries. *J. Power Sources* **1999**, *81–82*, 656-660.
- Gillot, B.; Domenichini, B.; Tailhades, P.; Bouet, L.; Rousset, A., Reactivity of the submicron molybdenum ferrites towards oxygen and formation of new cation deficient spinels. *Solid State Ion.* **1993**, *63*, 620-627.
- Hahn, B. P.; Long, J. W.; Mansour, A. N.; Pettigrew, K. A.; Osofsky, M. S.; Rolison, D. R., Electrochemical Li-ion storage in defect spinel iron oxides: the critical role of cation vacancies. *Energy Environ. Sci.* **2011**, *4*, 1495-1502.
- Swider-Lyons, K. E.; Love, C. T.; Rolison, D. R., Improved lithium capacity of defective V_2O_5 materials. *Solid State Ion.* **2002**, *152–153*, 99-104.
- Li, W.; Corradini, D.; Body, M.; Legein, C.; Salanne, M.; Ma, J.; Chapman, K. W.; Chupas, P. J.; Rollet, A.-L.; Julien, C.; Zhagib, K.; Duttine, M.; Demourgues, A.; Groult, H.; Dambournet, D., High Substitution Rate in TiO_2 Anatase Nanoparticles with Cationic Vacancies for Fast Lithium Storage. *Chem. Mater.* **2015**, *27*, 5014-5019.
- Li, W.; Body, M.; Legein, C.; Borkiewicz, O. J.; Dambournet, D., Atomic Insights into Nanoparticle Formation of Hydroxyfluorinated Anatase Featuring Titanium Vacancies. *Inorg. Chem.* **2016**, *55*, 7182-7187.
- Whittingham, M. S.; Dines, M. B., n-Butyllithium—An Effective, General Cathode Screening Agent. *J. Electrochem. Soc.* **1977**, *124*, 1387-1388.
- Chupas, P. J.; Chapman, K. W.; Lee, P. L., Applications of an amorphous silicon-based area detector for high-resolution, high-sensitivity and fast time-resolved pair distribution function measurements. *J. Appl. Crystal.* **2007**, *40*, 463-470.
- Chupas, P. J.; Qiu, X.; Hanson, J. C.; Lee, P. L.; Grey, C. P.; Billinge, S. J. L., Rapid-acquisition pair distribution function (RA-PDF) analysis. *J. Appl. Crystal.* **2003**, *36*, 1342-1347.
- Hammersley, A. P.; Svensson, S. O.; Hanfland, M.; Fitch, A. N.; Hausermann, D., Two-dimensional detector software: From real detector to idealised image or two-theta scan. *High Pres. Res.* **1996**, *14*, 235-248.
- Qiu, X.; Thompson, J. W.; Billinge, S. J. L., PDFgetX2: a GUI-driven program to obtain the pair distribution function from X-ray powder diffraction data. *J. Appl. Crystal.* **2004**, *37*, 678.
- Farrow, C. L.; Juhas, P.; Liu, J. W.; Bryndin, D.; Božin, E. S.; Bloch, J.; Th, P.; Billinge, S. J. L., PDFfit2 and PDFgui: computer programs for studying nanostructure in crystals. *J. Phys. Condens. Matter* **2007**, *19*, 335219.
- Massiot, D.; Fayon, F.; Capron, M.; King, I.; Le Calvé, S.; Alonso, B.; Durand, J.-O.; Bujoli, B.; Gan, Z.; Hoatson, G., Modelling one- and two-dimensional solid-state NMR spectra. *Magn. Reson. Chem.* **2002**, *40*, 70-76.
- Kresse, G.; Hafner, J., Norm-conserving and ultrasoft pseudopotentials for first-row and transition elements. *J. Phys. Condens. Matter* **1994**, *6*, 8245-8257.
- Kresse, G.; Furthmüller, J., Efficiency of ab-initio total energy calculations for metals and semiconductors using a plane-wave basis set. *Comput. Mater. Sci.* **1996**, *6*, 15-50.
- Kresse, G.; Joubert, D., From ultrasoft pseudopotentials to the projector augmented-wave method. *Phys. Rev. B* **1999**, *59*, 1758-1775.

19. Dudarev, S. L.; Liechtenstein, A. I.; Castell, M. R.; Briggs, G. A. D.; Sutton, A. P., Surface states on NiO (100) and the origin of the contrast reversal in atomically resolved scanning tunneling microscope images. *Phys. Rev. B* **1997**, *56*, 4900-4908.
20. Dudarev, S. L.; Botton, G. A.; Savrasov, S. Y.; Humphreys, C. J.; Sutton, A. P., Electron-energy-loss spectra and the structural stability of nickel oxide: An LSDA+U study. *Phys. Rev. B* **1998**, *57*, 1505-1509.
21. Morgan, B. J.; Watson, G. W., GGA+U description of lithium intercalation into anatase TiO₂. *Phys. Rev. B* **2010**, *82*, 144119.
22. Morgan, B. J.; Watson, G. W., Role of Lithium Ordering in the Li_xTiO₂ Anatase → Titanate Phase Transition. *J. Phys. Chem. Lett.* **2011**, *2*, 1657-1661.
23. Morgan, B. J.; Madden, P. A., Lithium intercalation into TiO₂(B): A comparison of LDA, GGA, and GGA+U density functional calculations. *Phys. Rev. B* **2012**, *86*, 035147.
24. Koketsu, T.; Ma, J.; Morgan, B. J.; Body, M.; Legein, C.; Dachraoui, W.; Giannini, M.; Demortiere, A.; Salanne, M.; Dardoize, F.; Groult, H.; Borkiewicz, O. J.; Chapman, K. W.; Strasser, P.; Dambournet, D., Reversible magnesium and aluminium ions insertion in cation-deficient anatase TiO₂. *Nat. Mater.* **2017**, *16*, 1142-1148.
25. Corradini, D.; Dambournet, D.; Salanne, M., Tuning the Electronic Structure of Anatase Through Fluorination. *Sci. Rep.* **2015**, *5*, 11553.
26. Morgan, B. J., DFT dataset: X=(Li,Na,Ca,Mg,Al) Intercalation into (F/OH)-Substituted Anatase TiO₂. *University of Bath Data Archive* **2017**, doi: 10.15125/BATH-00473.
27. Morgan, B. J., DFT Data Analysis: Intercalation of X=(Li, Na, Mg, Ca, Al) into (F/OH)-substituted anatase TiO₂. *Zenodo* **2017**, <http://doi.org/10.5281/zenodo.1181872>.
28. Li, W.; Body, M.; Legein, C.; Borkiewicz, O.; Dambournet, D., Solvothermal Temperature Drives Morphological and Compositional changes through De-Hydroxyfluorination in Anatase Nanoparticles. *Eur. J. Inorg. Chem.* **2017**, *2017*, 192-197.
29. Chapman, K. W., Emerging operando and x-ray pair distribution function methods for energy materials development. *MRS Bull.* **2016**, *41*, 231-240.
30. Gao, P.; Metz, P.; Hey, T.; Gong, Y.; Liu, D.; Edwards, D. D.; Howe, J. Y.; Huang, R.; Misture, S. T., The critical role of point defects in improving the specific capacitance of δ-MnO₂ nanosheets. *Nat. Commun.* **2017**, *8*, 14559.
31. Mikami, M.; Nakamura, S.; Kitao, O.; Arakawa, H., Lattice dynamics and dielectric properties of TiO₂ anatase: A first-principles study. *Phys. Rev. B* **2002**, *66*, 155213.
32. Ohsaka, T.; Izumi, F.; Fujiki, Y., Raman spectrum of anatase, TiO₂. *J. Raman Spectrosc.* **1978**, *7*, 321-324.
33. Balachandran, U.; Eror, N. G., Raman spectra of titanium dioxide. *J. Solid State Chem.* **1982**, *42*, 276-282.
34. Frank, O.; Zukalova, M.; Laskova, B.; Kurti, J.; Koltai, J.; Kavan, L., Raman spectra of titanium dioxide (anatase, rutile) with identified oxygen isotopes (16, 17, 18). *Phys. Chem. Chem. Phys.* **2012**, *14*, 14567-14572.
35. Kavan, L.; Zukalova, M.; Ferus, M.; Kurti, J.; Koltai, J.; Civis, S., Oxygen-isotope labeled titania: Ti₁₈O₂. *Phys. Chem. Chem. Phys.* **2011**, *13*, 11583-11586.
36. Giarola, M.; Sanson, A.; Monti, F.; Mariotto, G.; Bettinelli, M.; Speghini, A.; Salviulo, G., Vibrational dynamics of anatase TiO₂: Polarized Raman spectroscopy and ab initio calculations. *Phys. Rev. B* **2010**, *81*, 174305.
37. Mazzolini, P.; Russo, V.; Casari, C. S.; Hitosugi, T.; Nakao, S.; Hasegawa, T.; Li Bassi, A., Vibrational-Electrical Properties Relationship in Donor-Doped TiO₂ by Raman Spectroscopy. *J. Phys. Chem. C* **2016**, *120*, 18878-18886.
38. Fu, Y.; Du, H.; Zhang, S.; Huang, W., XPS characterization of surface and interfacial structure of sputtered TiNi films on Si substrate. *Mater. Sci. Eng. A* **2005**, *403*, 25-31.
39. Yu, J. C.; Yu; Ho; Jiang; Zhang, Effects of F⁻ Doping on the Photocatalytic Activity and Microstructures of Nanocrystalline TiO₂ Powders. *Chem. Mater.* **2002**, *14*, 3808-3816.
40. Yang, H. G.; Sun, C. H.; Qiao, S. Z.; Zou, J.; Liu, G.; Smith, S. C.; Cheng, H. M.; Lu, G. Q., Anatase TiO₂ single crystals with a large percentage of reactive facets. *Nature* **2008**, *453*, 638-641.
41. Le, T. K.; Flahaut, D.; Martinez, H.; Pigot, T.; Nguyen, H. K. H.; Huynh, T. K. X., Surface fluorination of single-phase TiO₂ by thermal shock method for enhanced UV and visible light induced photocatalytic activity. *Appl. Catal. B* **2014**, *144*, 1-11.
42. Sudant, G.; Baudrin, E.; Larcher, G.; Tarascon, J.-M., Electrochemical lithium reactivity with nanotextured anatase-type TiO₂. *J. Mater. Chem.* **2005**, *15*, 1263-1269.
43. Borghols, W. J. H.; Lutzenkirchen-Hecht, D.; Haake, U.; van Eck, E. R. H.; Mulder, F. M.; Wagemaker, M., The electronic structure and ionic diffusion of nanoscale LiTiO₂ anatase. *Phys. Chem. Chem. Phys.* **2009**, *11*, 5742-5748.
44. Fehse, M.; Monconduit, L.; Fischer, F.; Tessier, C.; Stievano, L., Study of the insertion mechanism of lithium into anatase by operando X-ray diffraction and absorption spectroscopy. *Solid State Ion.* **2014**, *268*, 252-255.
45. Wagemaker, M.; Borghols, W. J. H.; Mulder, F. M., Large Impact of Particle Size on Insertion Reactions. A Case for Anatase Li_xTiO₂. *J. Amer. Chem. Soc.* **2007**, *129*, 4323-4327.
46. Sadoc, A.; Body, M.; Legein, C.; Biswal, M.; Fayon, F.; Rocquefelte, X.; Boucher, F., NMR parameters in alkali, alkaline earth and rare earth fluorides from first principle calculations. *Phys. Chem. Chem. Phys.* **2011**, *13*, 18539-18550.
47. Wang, J.; Polleux, J.; Lim, J.; Dunn, B., Pseudocapacitive Contributions to Electrochemical Energy Storage in TiO₂ (Anatase) Nanoparticles. *J. Phys. Chem. C* **2007**, *111*, 14925-14931.
48. Kavan, L., Lithium insertion into TiO₂ (anatase): electrochemistry, Raman spectroscopy, and isotope labeling. *J. Solid State Electrochem.* **2014**, *18*, 2297-2306.
49. Shen, K.; Chen, H.; Klaver, F.; Mulder, F. M.; Wagemaker, M., Impact of Particle Size on the Non-Equilibrium Phase Transition of Lithium-Inserted Anatase TiO₂. *Chem. Mater.* **2014**, *26*, 1608-1615.
50. Melot, B. C.; Tarascon, J. M., Design and Preparation of Materials for Advanced Electrochemical Storage. *Acc. Chem. Res.* **2013**, *46*, 1226-1238.
51. Fattakhova, D.; Kavan, L.; Krttil, P., Lithium insertion into titanium dioxide (anatase) electrodes: microstructure and electrolyte effects. *J. Solid State Electrochem.* **2001**, *5*, 196-204.
52. Wen, C. J.; Boukamp, B. A.; Huggins, R. A.; Weppner, W., Thermodynamic and Mass Transport Properties of "LiAl". *J. Electrochem. Soc.* **1979**, *126*, 2258-2266.
53. Van der Ven, A.; Bhattacharya, J.; Belak, A. A., Understanding Li Diffusion in Li-Intercalation Compounds. *Acc. Chem. Res.* **2013**, *46*, 1216-1225.
54. Lantelme, F.; Mantoux, A.; Groult, H.; Lincot, D., Analysis of a phase transition process controlled by diffusion, application to lithium insertion into V₂O₅. *Electrochim. Acta* **2002**, *47*, 3927-3938.
55. Darken, L. S., Diffusion, mobility and their interrelation through free energy in binary metallic systems. *Trans. AIME* **1951**, *175*, 184-201.
56. Shewmon, P. G., *Diffusion In Solids*. McGraw-Hill: New York, 1963.
57. Weppner, W.; Huggins, R. A., Determination of the Kinetic Parameters of Mixed-Conducting Electrodes and Application to the System Li₃Sb. *J. Electrochem. Soc.* **1977**, *124*, 1569-1578.

58. Lantelme, F.; Mantoux, A.; Groult, H.; Lincot, D.,
Electrochemical Study of Phase Transition Processes in
Lithium Insertion in V_2O_5 Electrodes. *J. Electrochem. Soc.*
2003, *150*, A1202-A1208.

59. Lantelme, F.; Mantoux, A.; Groult, H.; Lincot, D.,
Electrochemical study of phase transition processes in lithium
batteries. *Solid State Ion.* **2006**, *177*, 205-209.

Table of Contents

